

# Simulation of a Variety of Wings using a Reynolds Stress Model

K. B. Thompson<sup>i</sup>

*North Carolina State University, Raleigh, NC, 27695-7910*

H. A. Hassan<sup>ii</sup>

*North Carolina State University, Raleigh, NC, 27695-7910*

**The Wilcox 2006 stress- $\omega$  model, a Reynolds stress model (RSM), implemented in both the NASA Langley codes FUN3D and CFL3D have been used to study a number of 2-D and 3-D cases. This study continues the assessments of the stress- $\omega$  model by simulating the flow over two wings: the DPW-W1 and the DLR-F11 wings. Using FUN3D, which uses unstructured grids, and CFL3D, which uses structured grid, the results were compared to solvers employing one- and two-equation turbulence models and experimental data. In general, in situations where experimental data is available, the stress- $\omega$  model performs as well or better than one- and two-equation models.**

## Nomenclature

AR	=	wing aspect ratio
b	=	wing full span
$C_{ref}$	=	wing mean aerodynamic chord (MAC)
$C_p$	=	pressure coefficient
M	=	Mach number
Re	=	Reynolds number
$S_{ref}$	=	wing reference area
$T_{ref}$	=	reference temperature
$X_{ref}$	=	x-direction pitching moment reference
$Y_{ref}$	=	y-direction pitching moment reference
$Z_{ref}$	=	z-direction pitching moment reference
$\alpha$	=	angle of attack
$\chi$	=	U-MUSCL scheme coefficient

<sup>i</sup> Graduate Research Assistant, Mechanical and Aerospace Engineering, Student Member AIAA

<sup>ii</sup> Professor, Mechanical and Aerospace Engineering, Fellow AIAA

## I. Introduction

Simulating flows over wing geometries has been studied extensively. Researchers have applied one- and two-equation turbulence models to predict many flow features, but these results may not always be satisfactory. Turbulent Reynolds stress (RSM) models offer a variety of appealing features: not relying on the linear relationship between Reynolds stress and strain rate tensor, they include the effects of curvature and rotation and resolve the normal stress anisotropy near walls.. The purpose of this study is to determine whether a Reynolds stress model can provide more accurate results in simulating flow over complex wing shape using different grids and flow solvers. In an earlier investigation<sup>1</sup>, the Wilcox 2006 stress- $\omega$  model<sup>2</sup> was used to study a variety of two-dimensional flows and the ONERA and NASA Trapezoidal wing, using CFL3D<sup>3</sup>.

For the work in this paper, the Wilcox 2006 stress- $\omega$  model<sup>2</sup> is used to simulate other wings. The model is a second-moment RSM consisting of five mean-flow conservation equations, six stress equations, and one length scale equation. The stress- $\omega$  model is largely distinguished from other second-moment RSMs by its length scale equation. Where other models, such as the Launder-Reece-Rodi (LRR)<sup>4</sup> model, are based upon the  $\epsilon$ -equation, the stress- $\omega$  length scale equation is based upon the  $\omega$ -equation, and thus avoids the problems near the wall associated with the  $\epsilon$ -equation. This RSM was recently implemented into the NASA Langley FUN3D<sup>5</sup> code and validated with extensive comparison to test cases available on the NASA Langley Turbulence Modeling Resource website<sup>1</sup>.

This research focuses on two wings, the DPW-W1 wing from the 3<sup>rd</sup> AIAA Drag Prediction Workshop<sup>6</sup> and the DLR-F11 wing from the 2<sup>nd</sup> High Lift Prediction Workshop<sup>7</sup>. These two wings represent a cruise-type configuration and a high-lift configuration representative of realistic aircraft configurations. The 3<sup>rd</sup> AIAA Drag Prediction Workshop conducted an extensive study on the DPW-W1 wing, with flow simulation done by a wide variety of structured and unstructured flow solvers. A statistical framework was used to validate the results, and all results made available. These results included pressure and skin friction coefficient predictions at various span-wise positions. The 2<sup>nd</sup> High Lift Prediction Workshop also conducted a similar study, and also collected experimental data from two wind tunnel facilities.

## II. Wing Geometries

The DPW-W1 is a simple wing-alone model, designed to be representative of a supercritical section found on most transport aircraft, and it is shown in figure 1. The key features of the this wing are given as follows

$S_{ref}$	290322mm <sup>2</sup>	$X_{ref}$	154.245 mm
$C_{ref}$	197.556 mm	$Y_{ref}$	0.0 mm
$b/2$	762 mm	$Z_{ref}$	0.0 mm
AR	8.0		

<sup>1</sup><http://turbmodels.larc.nasa.gov/>

All moment reference coordinates are based on an origin at the wing root leading edge. No flap or aircraft fuselage is attached to this wing, and simulation was conducted as though in a free-air environment.

The DLR-F11 model represents a three element high lift wing configuration in landing configuration and an attached body pod, shown in figures 2 and 3. The model included slat and flap track fairings that will hence be referred to as “brackets”. The key features of this wing-body configuration are given as follows

$S_{ref}$	419130 mm <sup>2</sup>	$X_{ref}$	1428 mm
$C_{ref}$	347.09 mm	$Y_{ref}$	0.0 mm
$b/2$	1400 mm	$Z_{ref}$	-41.61 mm
AR	9.353		

The moment reference coordinates are based on an origin at the nose of the body pod. The 2<sup>nd</sup> AIAA High Lift Prediction Workshop included data taken from two wind tunnels. A lower Reynolds number flight condition of 1.35 million was conducted in the low-speed wind tunnel Airbus-Deutschland (B-LSWT), and a high Reynolds number flight condition of 15.1 million was conducted at the European Transonic Windtunnel (ETW)<sup>7</sup>. Both facilities collected a large amount of pressure, velocity, and force/moment data, as well as oil flow visualizations.

### III. Test Conditions and Grid Systems

The 3<sup>rd</sup> AIAA Drag Prediction Workshop focused on solver-to-solver comparison for transonic flow. The DPW-W1 test conditions were  $Re = 15.16 \times 10^6$  (based on DPW-W1  $C_{ref}$ ),  $M = 0.175$ ,  $T_{ref} = 322$  K,  $\alpha = 0.5$  degrees. The grid used was an unstructured tetrahedral mesh generated by the NASA Langley Research Center. The grid was designed to be used by nodal-based flow solvers and consisted of 11.5 million points. This grid was previously used by FUN3D in the workshop, with the Spalart-Allmaras turbulence model<sup>8</sup>.

The 2<sup>nd</sup> AIAA High Lift Prediction Workshop focused on the lower-speed, landing stage of flight. The DLR-F11 high Reynolds number test conditions were  $Re = 15.1 \times 10^6$  (based on DLR-F11  $C_{ref}$ ),  $M = 0.175$ ,  $T_{ref} = 114.0$  K,  $\alpha = 7.16$  degrees. The lower Reynolds number test conditions were identical to the previous test conditions, except for  $Re = 1.35 \times 10^6$  (also based on DLR-F11  $C_{ref}$ ) and  $T_{ref} = 298.6$  K. For FUN3D, the grids used were the mixed element “D” medium grids, generated by Cessna and the University of Wyoming. The grids were created by merging the pure tetrahedral “D” medium grid with prisms in the boundary layer. For the high Reynolds number case, the grid did not include brackets, and consisted of 30.8 million nodes. For the low Reynolds number case, the grid included brackets and consisted of 41.5 million grid points. Both were previously used by FUN3D in the workshop, with the Spalart-Allmaras turbulence model. For CFL3D, the grid used was the structured “A” grid, generated by Boeing. The grid did not include brackets, consisted of 34.3 million points, and was previously used in CFL3D with the Spalart-Allmaras turbulence model.

## IV. Computational Approach

FUN3D is an unstructured, nodal-based, parallel 3-D compressible finite-volume grid code, which is capable of using mixed element meshes. An upwind Roe<sup>9</sup> scheme is used in this study, and second order accuracy is obtained by updating face values using a U-MUSCL scheme<sup>10</sup> with the  $\chi$  set as 0.5 for both cases. All gradients at mesh vertices are computed using a least-squares technique. Time-stepping is done based on a backwards Euler time differencing scheme. The linear system of equations is solved with a line implicit procedure that is used as a preconditioner for Generalized Conjugate Residual<sup>11</sup> (GCR), which helps to stabilize and accelerate convergence. No limiter was used for the DLR-F11 case or the DPW-W1 case, as it was not needed. The turbulence equations are solved separately from the mean flow equations.

CFL3D is a structured, cell-centered, parallel 3-D compressible finite-volume grid code. An upwind Roe flux difference-splitting method<sup>9</sup> is used in this study, with third-order spatial differencing used to compute the convective terms, and second-order central differencing used to compute the viscous terms. The turbulence equations are solved separately from the mean flow equations, using a first-order advection scheme, and time advancement is based on a backward Euler scheme, with an implicit approximate factorization method.

## V. Results

### DPW-W1

Figure 4 shows the comparison of pressure coefficients at various span positions along the wing. Since no experimental data was collected for this geometry, a solver-to-solver comparison is made to demonstrate consistency. The comparison is made with FUN3D, which was previously run on the same grid in the 3<sup>rd</sup> AIAA Drag Prediction Workshop with the Spalart Allmaras turbulence model, and with the TAU<sup>12</sup> results from the 3<sup>rd</sup> AIAA Drag Prediction Workshop. TAU is another unstructured modular CFD code developed by DLR, and was run using the Spalart Allmaras turbulence model with the Edwards modification<sup>13</sup>. The TAU case was run on a hybrid grid consisting of 10.5 million points. There is strong agreement in the pressure coefficient between all of these solvers at all spanwise locations, with the exception of the location of the weak shock on the upper surface of the wing. The RSM predicts a shock further aft on the wing than both of the other codes. Since no experimental data is available for this grid, the accuracy of these solutions cannot be ascertained because of a lack of experimental results. Notwithstanding, there is consistency between the results, which helps validate the implementation of the RSM in FUN3D.

The skin friction coefficient comparison is shown in figure 5. The RSM results are consistent with the SA and SA-Edwards results from the FUN3D and TAU; however, the RSM is likely less dissipative than either of the aforementioned turbulence models, due to the oscillatory behavior seen before the weak shock. There is clearly shock-boundary layer interaction captured by all the models, and difference in predicted shock location is also apparent. Again, the consistency in the results helps validate the RSM implementation and test results are required to determine the accuracy of both the pressure and skin friction results.

The surface pressure coefficients for the high Re case are shown in figure 6, comparing the FUN3D simulations using the Spalart Allmaras, SST-V (SST<sup>14</sup> with a vorticity source term) and stress- $\omega$  turbulence models, as well as experimental data collected at the ETW facility. The RSM performs as well as the two-equation SST-V turbulence model in almost all cases, and out-performs the SA model in the out-board flap in figure 6f. However, all models show a lack of agreement with the experiment in the lower region of the slat, where separation takes place, and all models underpredicted  $C_p$  on the upper surface of the flap at  $2y/b=0.15$ , with the stress- $\omega$  model showing the highest departure from the experiment.

In order to check consistency between FUN3D and CFL3D, both were used with the RSM for the high Re case at 7 degrees angle of attack. Figure 7 shows marginal differences in the surface pressure coefficients, with CFL3D performing better at most locations, except the outboard flap region. These differences can be attributed to differences between the grids used by both solvers and to differences in how the algorithm is employed by both codes. CFL3D was previously used to simulate numerous 2-D and 3-D flows, and it was shown to perform well in comparison to one- and two-equation turbulence models<sup>1</sup>. It is encouraging that the FUN3D implementation of the RSM performs, on average, as well as the CFL3D implementation in calculating surface pressures.

No SST-V results from the second AIAA High Lift Prediction Workshop were available for the low Re case that included brackets, so a comparison is made between the FUN3D solutions employing the SA turbulence model and the RSM and the experimental surface pressure data, shown in figures 8 and 9. The RSM predicts surface pressures much closer to the experiment than the SA turbulence model in almost all cases. Figures 8e, 9e, and 9f show that the RSM performs especially well on the flap, particularly where the SA turbulence model significantly overpredicts the pressure at the higher angle of attack. Moreover, stress- $\omega$  shows better agreement with experiment on the slat. This is significant, because most codes in the 2<sup>nd</sup> AIAA High Lift Prediction Workshop had the greatest error in this region<sup>7</sup>.

For the low Re case, figure 10 shows both models do a good job predicting lift and drag up to 16 degrees angle of attack. At 18.5 degrees angle of attack, the SA turbulence model does a better job predicting the pitching moment, and the RSM does a better job predicting drag. These results are encouraging in that they show the RSM able to provide better drag prediction than the one-equation Spalart-Allmaras at high angle of attack, which we speculate is due to the effect of streamline curvature and normal stress, both of which are both included in the RSM, but not in the SA turbulence model.

Figure 11 shows a sketch of the locations where velocities were measured using particle image velocimetry (PIV) in the B-LSWT wind tunnel. Figures 12 through 14 show comparisons of representative velocity profiles. Both models do poorly in comparison to the experimental measurement. There is very little difference overall in the predictions of either model where the effects of the wake are very small. Overall, the RSM does perform better than the SA turbulence model at the outboard stations, especially in the presence of a large wake, whereas the SA turbulence model better matches the experimental data at the inboard stations.

Convergence of the RSM was shown to differ between the two geometries. Figures 15 and 16 show the convergence of normalized residuals and lift and drag coefficients for FUN3D. In both figures, the mean flow and turbulence equation normalized residuals were computed as  $l^2$ -norms to best represent the total residual. Figure 15 shows the mean flow and turbulence equation residuals converged to nearly machine zero for double precision, and the lift and drag coefficients were both steady at convergence. Figure 16 shows that mean flow and turbulence equation residuals converged to the order of  $10^{-3}$  and  $10^{-4}$ , respectively. It should also be noted that for the DLR-F11 configuration, FUN3D had to be run past the point of the lift and drag coefficients reaching a steady value to obtain a converged solution for the velocity profiles, and it was typical to run FUN3D for greater than 20,000 iterations to achieve convergence.

## VI. Concluding Remarks

Overall this study of the stress- $\omega$  RSM was conducted to further assess its ability to accurately simulate external flow over wings. The NASA Langley FUN3D and CFL3D codes were both used to simulate flow over the high-lift DLR-F11 configuration, with the focus of this paper being primarily on the FUN3D results. The DPW-W1 was representative of a wing-alone case in a cruise configuration, and was intended to show that RSM could give results consistent with results from the 3<sup>rd</sup> AIAA Drag Prediction Workshop. The wing surface pressure and skin friction coefficients predicted by the RSM were consistent with those of the SA turbulence model and other flow solvers, with notable difference in the predicted shock location. Further study would benefit from experimental measurements of the DPW-W1 wing configuration to assess the accuracy of these models in predicting the pressure and skin friction coefficients.

For the DLR-F11 wing-body high-lift configuration, the RSM results were largely encouraging. Overall, the RSM performed better than the one-equation Spalart-Allmaras turbulence model at the 18.5 degree angle of attack case in many predictions. The RSM predictions of  $C_p$  did better match the experimental measurements at an 18.5 degree angle of attack than the SA turbulence model, especially on the outboard flap. Also, the drag predicted by the RSM was much closer to the measured value at higher angles of attack than the SA turbulence model. The performance of both models was very poor overall in capturing the velocity profile measured in the B-LSWT; however, the RSM did do better in regions where the wake has influence, on the outboard flap.

It is also encouraging that both CFL3D and FUN3D are able to obtain a converged RSM solution for a complex wing geometry, that was largely similar. Since the RSM results clearly showed improvements over the SA turbulence model and performed comparably to the SST-V model, there is the cost-benefit question of whether the RSM is worth the extra computation. We believe that it is. The 2006 Wilcox Stress- $\omega$  model is shown here to be a robust turbulence model, and should be further studied to better assess its merits. Future studies leave open the possibility of collecting skin friction experimental data and comparing the RSM to other two-equation turbulence models to assess whether other models perform as well in the outboard flap of the DLR-F11 configuration, where the RSM seems to be most accurate.

## Acknowledgements

The research is supported in part by NASA Cooperative Agreement NNX11AI56A, funded under the Aeronautical Sciences Project of the Fundamental Aeronautics Program. Dr. Chris Rumsey is the Technical Monitor.

The authors would like to thank Chris Rumsey and Elizabeth Lee-Rausch of NASA Langley for their support with FUN3D and CFL3D, and providing additional results from the 2<sup>nd</sup> High Lift Prediction Workshop.

## References

- <sup>1</sup> Rodio, J. J., Xiao, X., Hassan, H. A., and Rumsey, C. L., "NASA Trapezoidal Wing Simulation using Stress- $\omega$  and One- and Two-Equation Turbulence Models", 52<sup>nd</sup> *Aerospace Sciences Meeting*, scitec-2014-0404, AIAA, 2014
- <sup>2</sup> Krist, S. L., Biedron, R. T., and Rumsey, C. L., "CFL3D User's Manual (Version 5.0)," NASA-TM-1998-208444, June 1998.
- <sup>3</sup> Wilcox, D. C., *Turbulence Modeling for CFD*, 3rd Edition, DCW Industries, LA Canada, CA, 2006.
- <sup>4</sup> Eisfeld, B. "Differential Reynolds Stress Modeling at DLR Status & Perspectives", presentation, NASA Langley Research Center, Hampton, VA, April 1, 2014.
- <sup>5</sup> FUN3D, Fully Unstructured Navier Stokes, NASA Langley Research Center, Hampton, VA, 2014.
- <sup>6</sup> Lee-Rausch, E. M., Rumsey C. L., and Hammond, D. P., "FUN3D Analysis of DPW-III Wing/Body Configurations," presentation, 3<sup>rd</sup> AIAA Drag Prediction Workshop, San Francisco, CA, June 3, 2006.
- <sup>7</sup> Rumsey, C. L., and Slotnick, J. P., Overview and Summary of the Second AIAA High Lift Prediction Workshop (Invited), AIAA Paper 2014-0747, 2014.
- <sup>8</sup> Spalart, P. R. and Allmaras, S. R., "A One-Equation Turbulence Model for Aerodynamic Flows," *Recherche Aerospatiale*, No. 1, 1994, pp.5-21.
- <sup>9</sup> Roe, P. L., "Approximate Riemann Solvers, Parameter Vectors, and Difference Schemes," *Journal of Computational Physics*, Vol. 43, 1981, pp. 357-372.
- <sup>10</sup> Burg, C. O. E., Sheng, C., Newman, III, J. C., Brewer, W., Blades, E., and Marcum, D. L., "Verification and Validation of Forces Generated by an Unstructured Flow Solver," AIAA Paper 2003-3983, 2003.
- <sup>11</sup> Stanley C. Eisenstat, Howard C. Elman and Martin H. Schultz, *SIAM Journal on Numerical Analysis*, Vol. 20, No. 2 (Apr., 1983), pp. 345-357
- <sup>12</sup> D. Schwamborn, T. Gerhold, R. Heinrich, "The DLR TAU-Code: Recent Applications in Research and Industry", Invited Lecture in Proceedings on CD of the European Conference on Computational Fluid Dynamics ECCOMAS CDF 2006, P. Wesseling, E. Oñate, J. Périaux (Eds), The Netherlands, 2006
- <sup>13</sup> Jack R. Edwards and Suresh Chandra. "Comparison of eddy viscosity-transport turbulence models for three-dimensional, shock-separated flowfields", *AIAA Journal*, Vol. 34, No. 4 (1996), pp. 756-763.
- <sup>14</sup> Menter, F. R., "Two-Equation Eddy-Viscosity Turbulence Models for Engineering Applications," *AIAA Journal*, Vol. 32, No. 8, 1994, pp. 1598-1605.

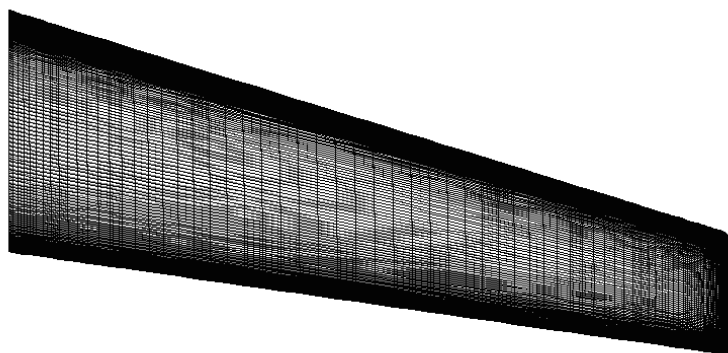


**Figure 1. DPW-W1 Surface Mesh**



**Figure 2. DLR-F11 model in the B-LWST wind tunnel**

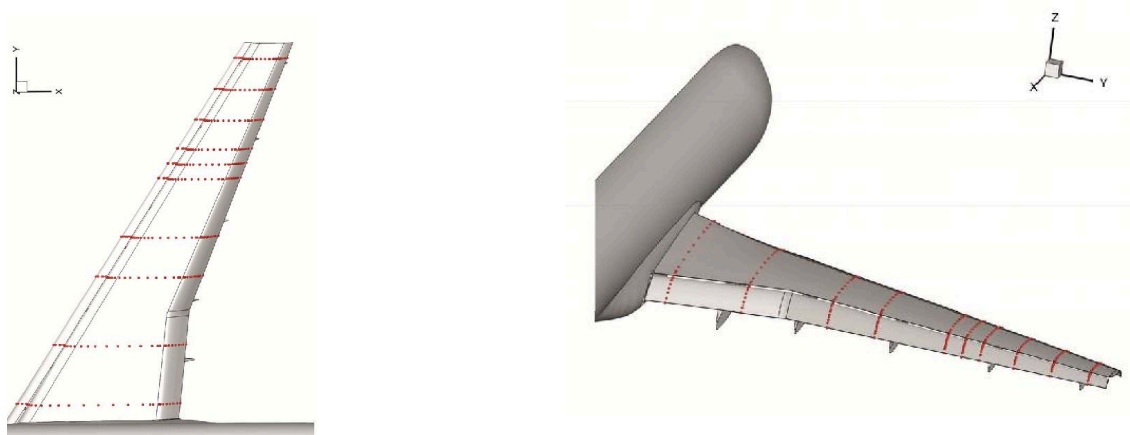
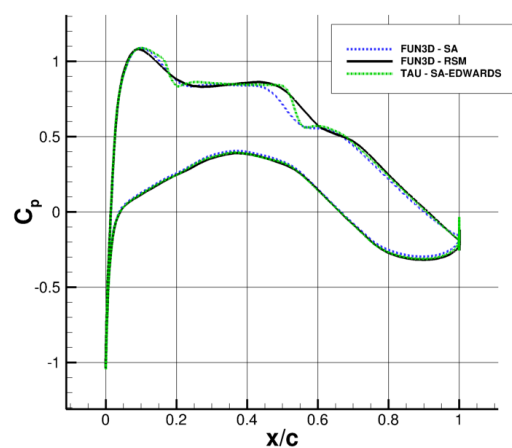
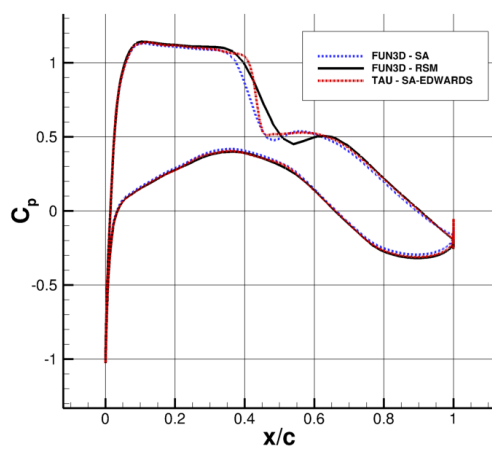


**Figure 3. DLR-F11 pressure tap locations**

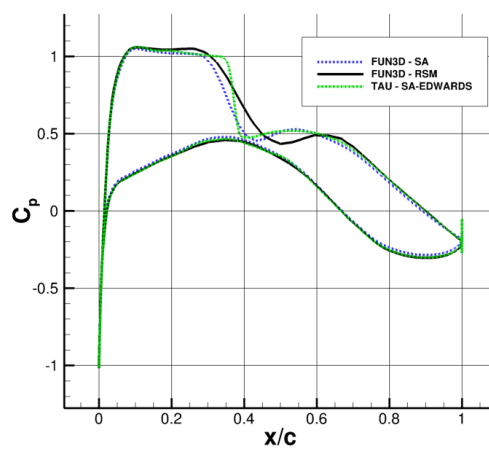




(a) DPW-W1 at  $y = 120$  mm

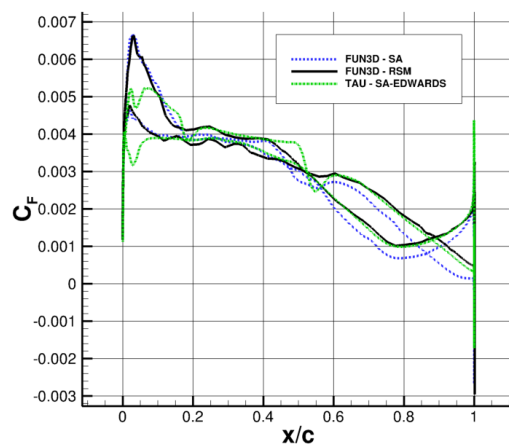


(b) DPW-W1 at  $y = 320$  mm

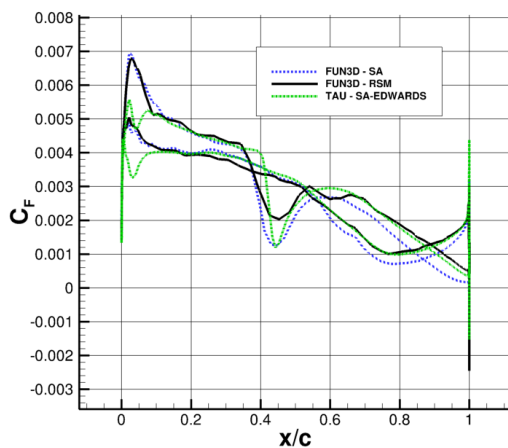


(c) DPW-W1 at  $y = 620$  mm

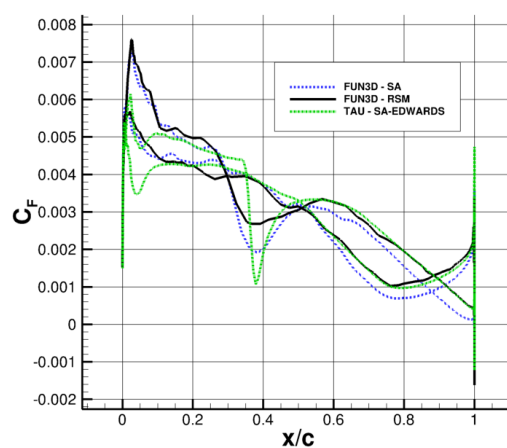
**Figure 4. Pressure coefficients at  $\alpha = 0.5^\circ$**



(b) DPW-W1 at  $y = 120$  mm

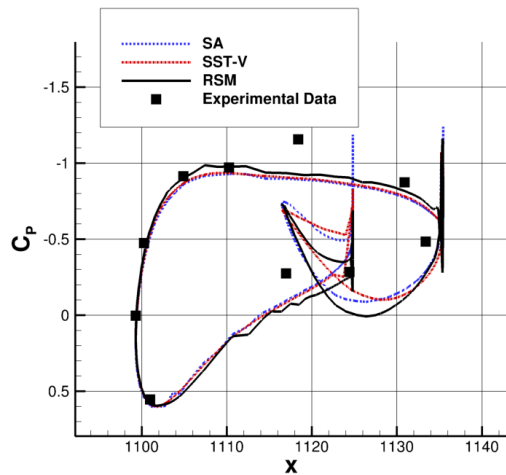


(b) DPW-W1 at  $y = 320$  mm

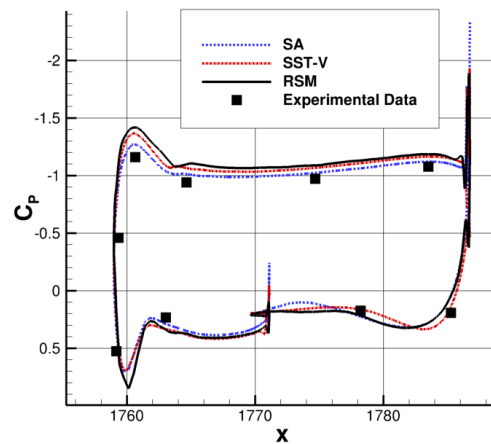


(c) DPW-W1 at  $y = 620$  mm

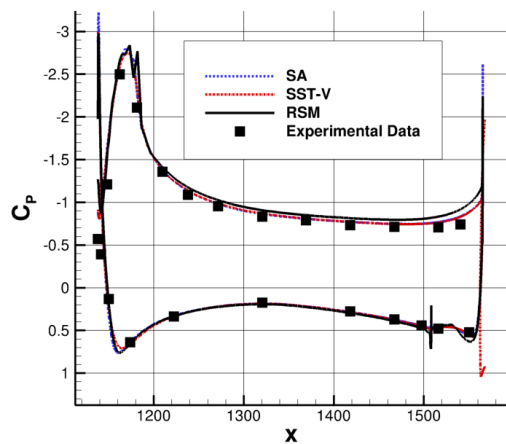
**Figure 5. Skin friction coefficients at  $\alpha = 0.5^\circ$**



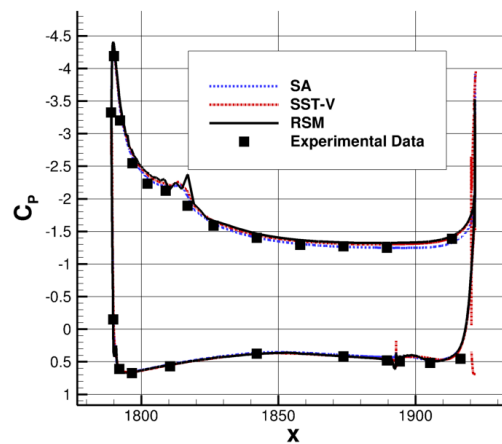
(a) Slat at  $2y/B = 0.15$ , no brackets



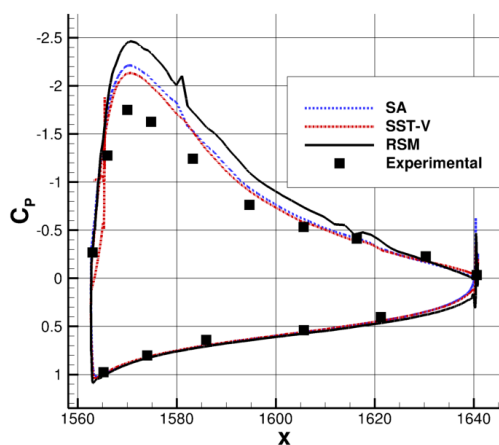
(b) Slat at  $2y/B = 0.89$ , no brackets



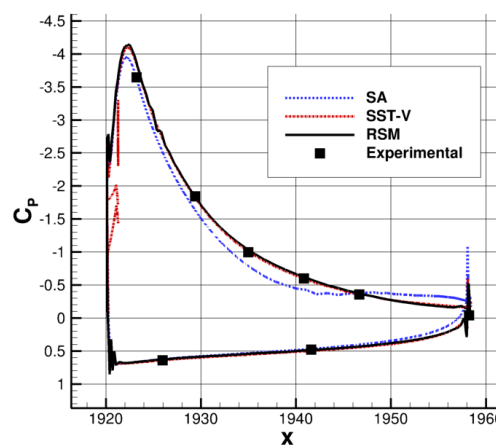
(c) Main wing at  $2y/B = 0.15$ , no brackets



(d) Main wing at  $2y/B = 0.89$ , no brackets

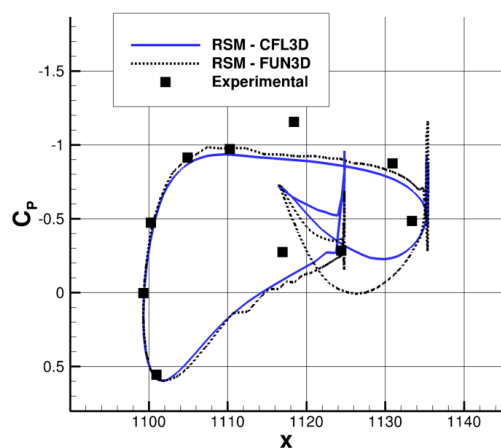
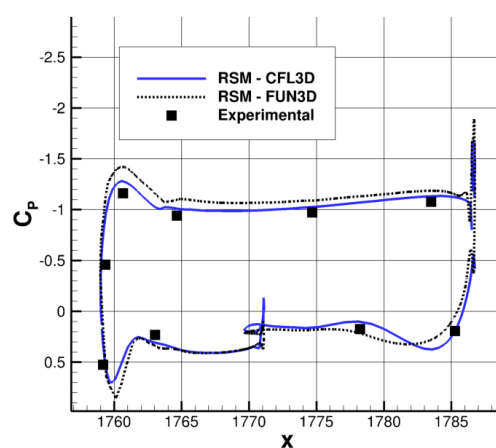
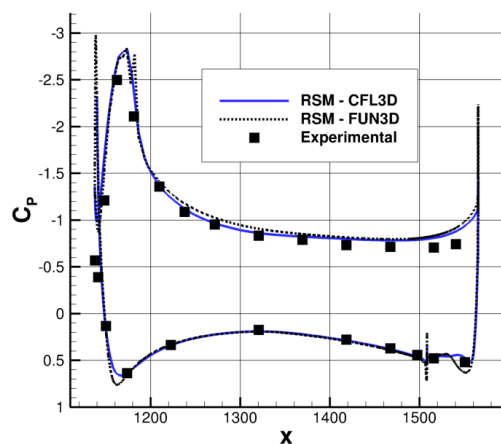
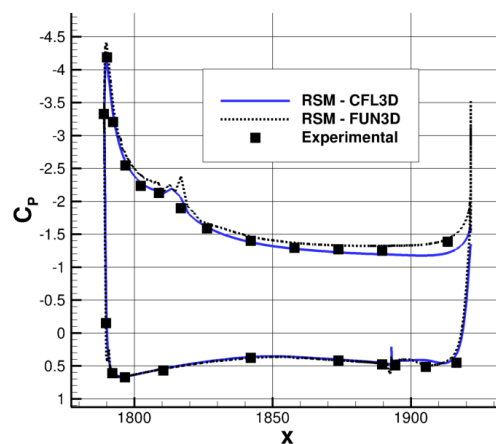
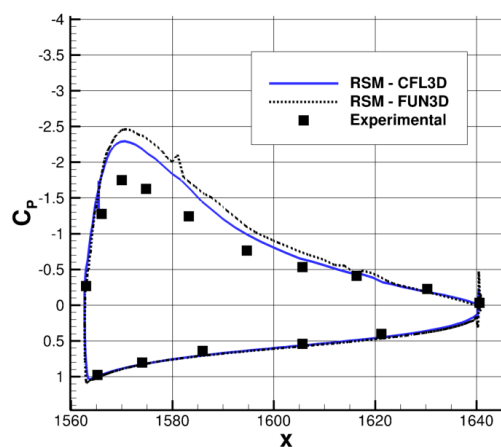
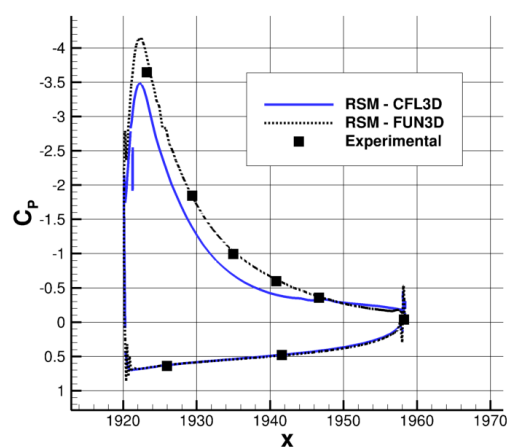


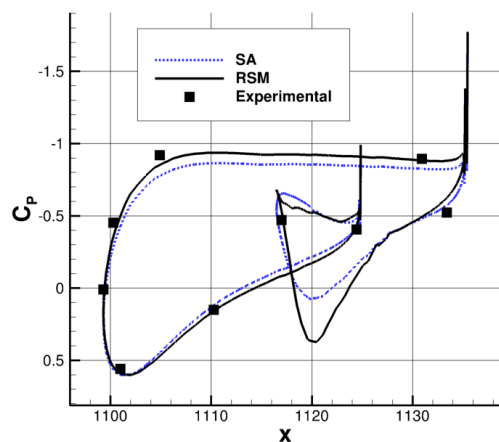
(e) Flap at  $2y/B = 0.15$ , no brackets



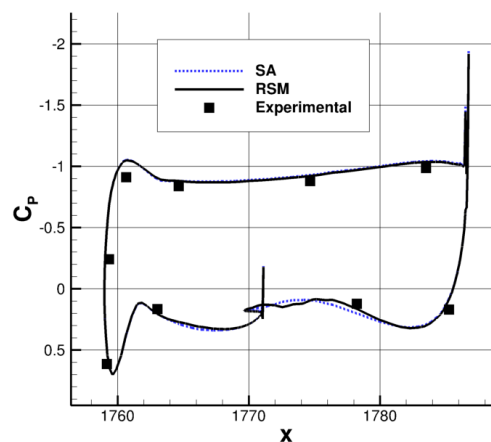
(f) Flap at  $2y/B = 0.89$

**Figure 6. Surface pressure coefficients for two span locations at  $\alpha = 7^\circ$ ,  $Re = 15.1 \times 10^6$**

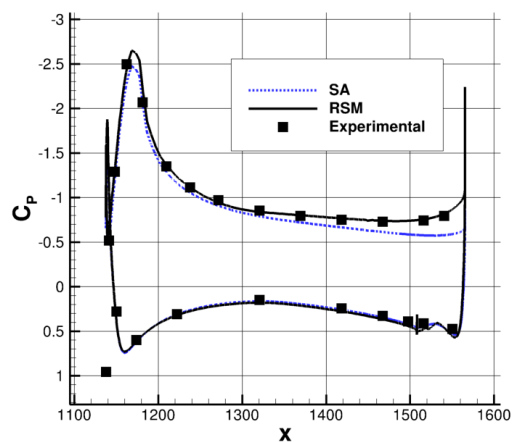
(a) Slat at  $2y/B = 0.15$ , no brackets(b) Slat at  $2y/B = 0.89$ , no brackets(c) Main wing at  $2y/B = 0.15$ , no brackets(d) Main wing at  $2y/B = 0.89$ , no brackets(e) Flap at  $2y/B = 0.15$ , no brackets(f) Flap at  $2y/B = 0.89$ **Figure 7. Surface pressure coefficients for two span locations at  $\alpha = 7^\circ$ ,  $Re = 15.1 \times 10^6$**



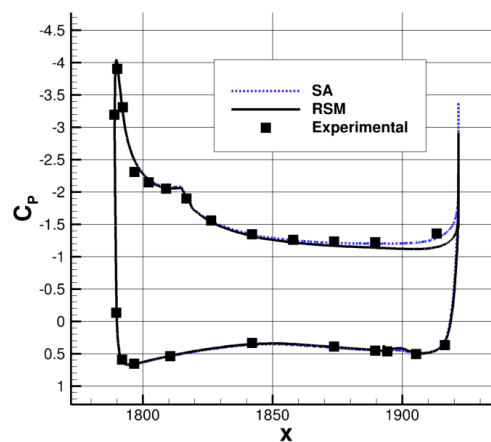
(a) Slat at  $2y/B = 0.15$ , w/brackets



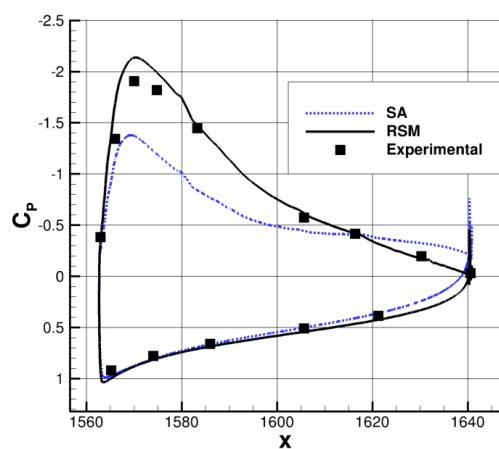
(b) Slat at  $2y/B = 0.89$ , w/brackets



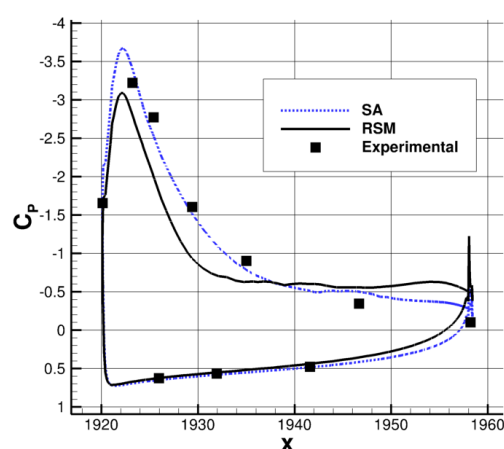
(c) Main wing at  $2y/B = 0.15$ , w/brackets



(d) Main wing at  $2y/B = 0.89$ , w/brackets

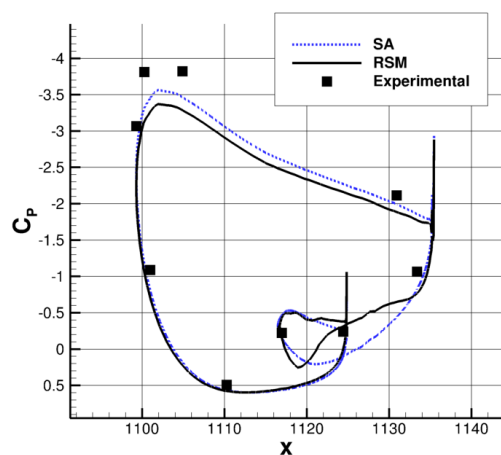


(e) Flap at  $2y/B = 0.15$ , w/brackets

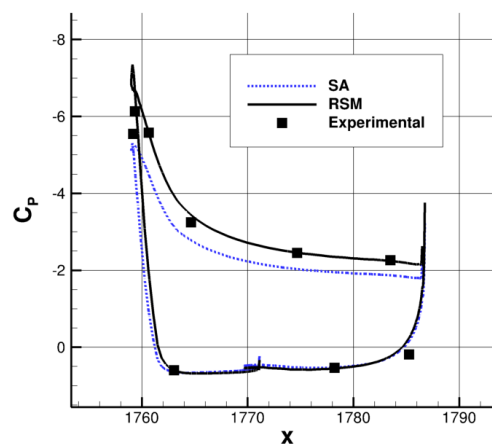


(f) Flap at  $2y/B = 0.89$ , w/brackets

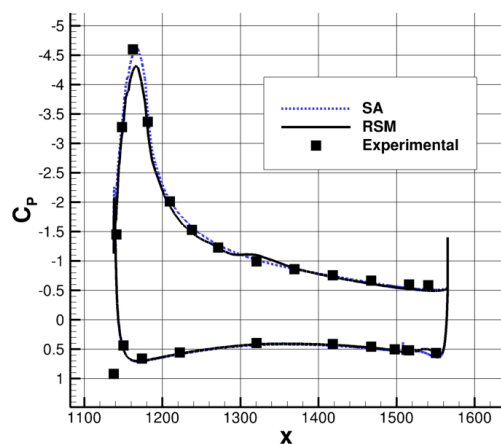
**Figure 8. Surface pressure coefficients for two span locations at  $\alpha = 7^\circ$ ,  $Re = 1.35 \times 10^6$**



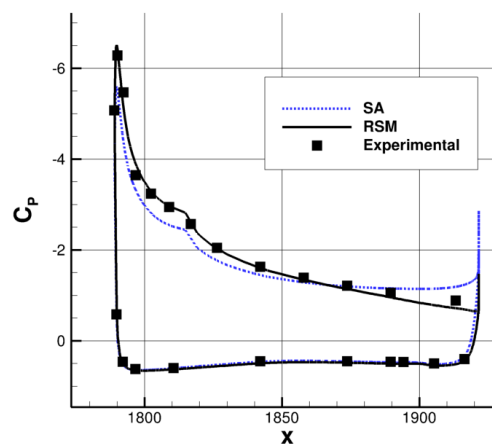
(a) Slat at  $2y/B = 0.15$ , w/brackets



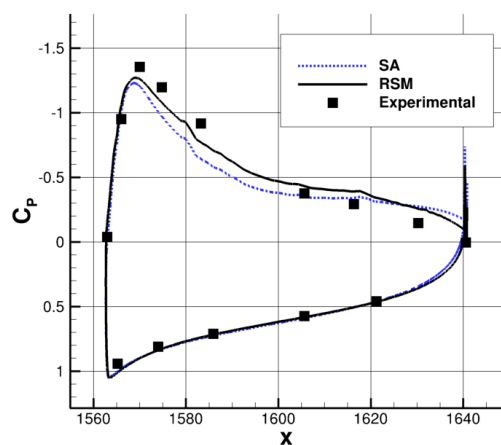
(b) Slat at  $2y/B = 0.89$ , w/brackets



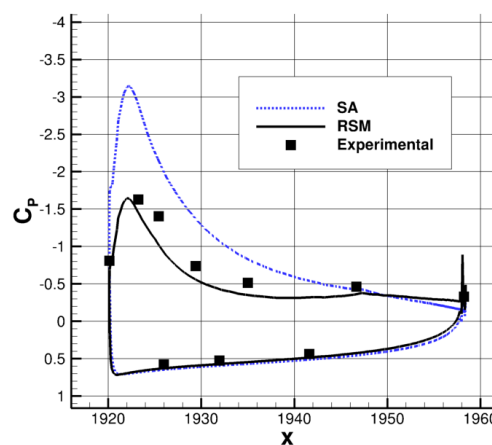
(c) Main wing at  $2y/B = 0.15$ , w/brackets



(d) Main wing at  $2y/B = 0.89$ , w/brackets



(e) Flap at  $2y/B = 0.15$ , w/brackets



(f) Flap at  $2y/B = 0.89$ , w/brackets

**Figure 9. Surface pressure coefficients at for two span locations at  $\alpha = 18.5^\circ$ ,  $Re = 1.35 \times 10^6$**

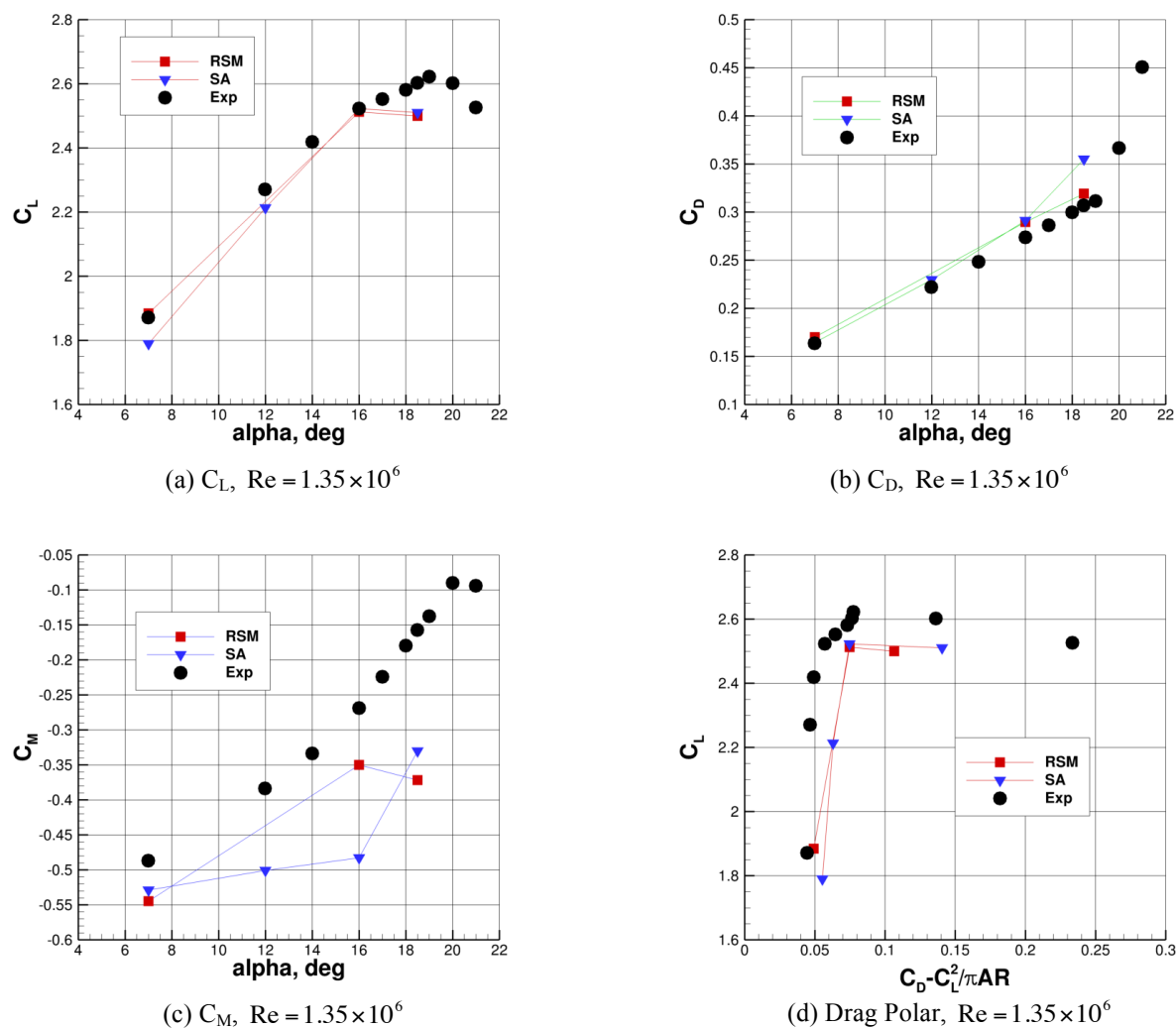


Figure 10. Forces and pitching moments (w/brackets)

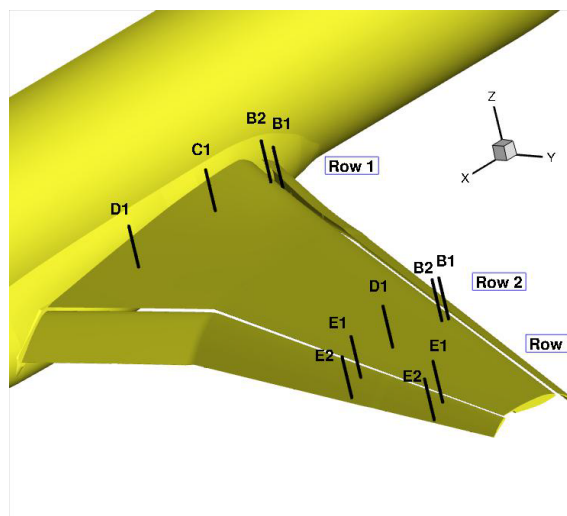
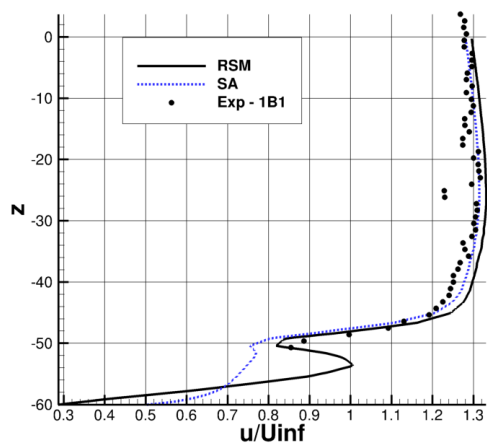
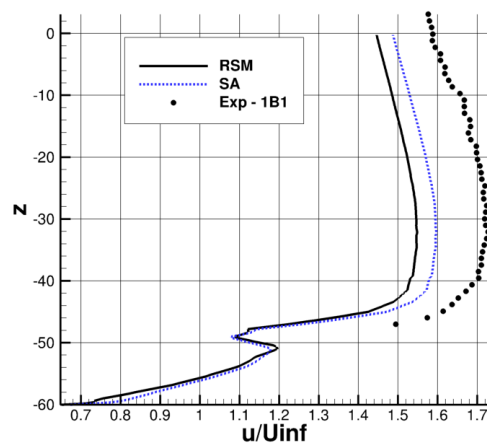


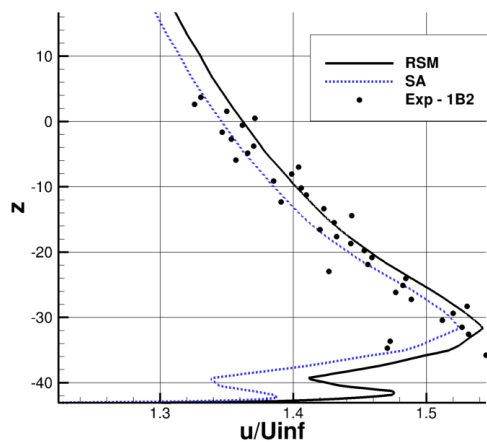
Figure 11. Velocity Profile Locations



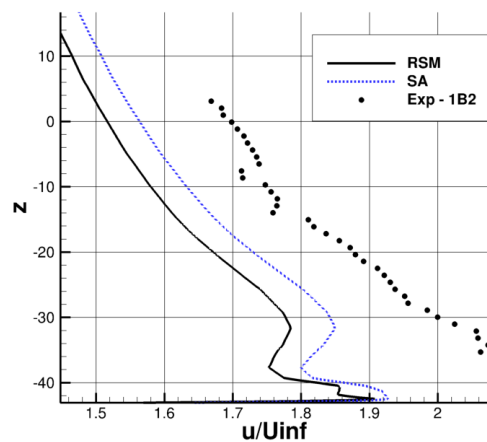
(a) Location 1B1 at  $\alpha = 7^\circ$ , w/brackets



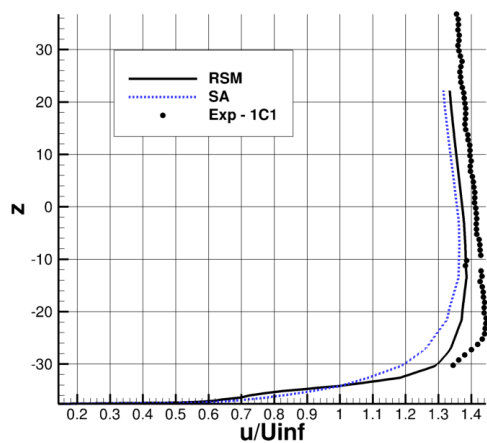
(b) Location 1B1 at  $\alpha = 18.5^\circ$ , w/brackets



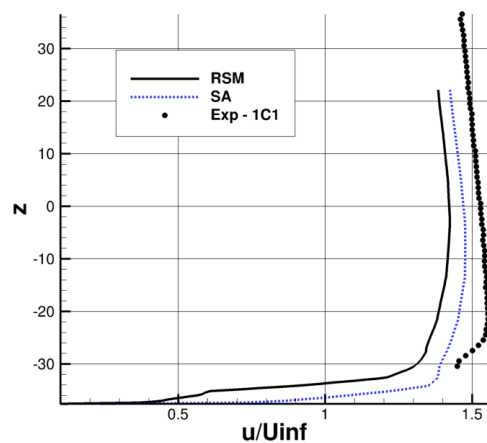
(c) Location 1B2 at  $\alpha = 7^\circ$ , w/brackets



(d) Location 1B2 at  $\alpha = 18.5^\circ$ , w/brackets



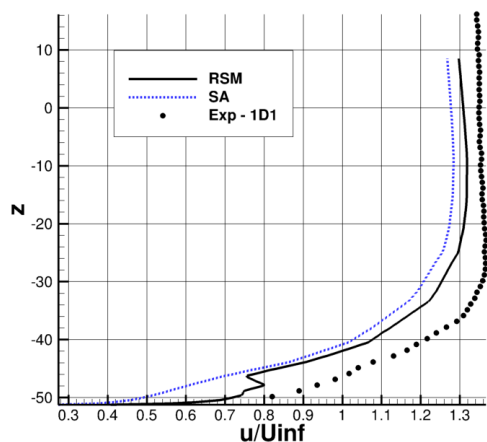
(e) Location 1C1 at  $\alpha = 7^\circ$ , w/brackets



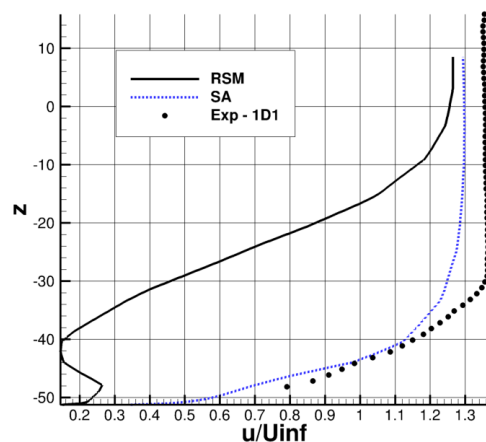
(f) Location 1C1 at  $\alpha = 18.5^\circ$ , w/brackets

**Figure 12. Velocity profiles (part 1) at  $Re = 1.35 \times 10^6$**

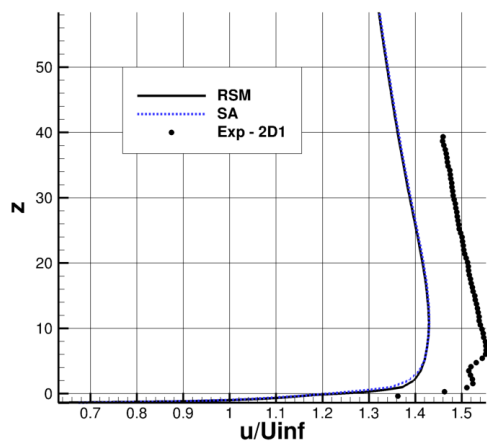




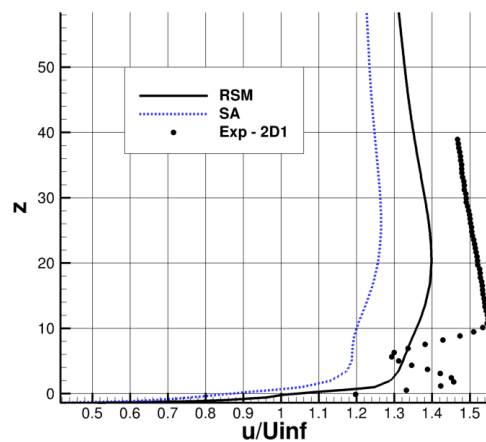
(a) Location 1D1 at  $\alpha = 7^\circ$ , w/brackets



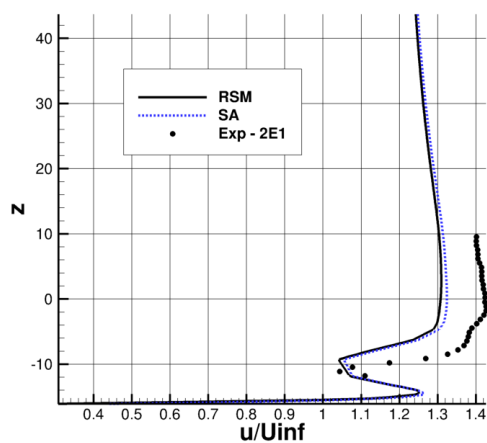
(b) Location 1D1 at  $\alpha = 18.5^\circ$ , w/brackets



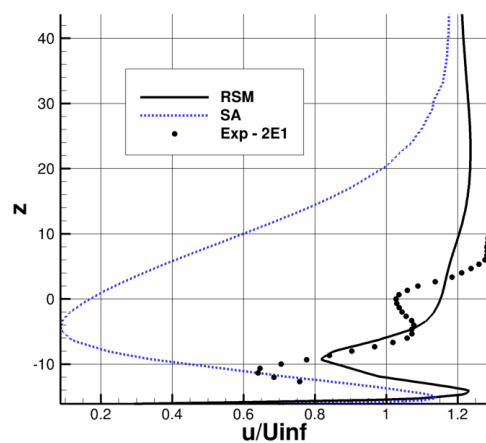
(c) Location 2D1 at  $\alpha = 7^\circ$ , w/brackets



(d) Location 2D1 at  $\alpha = 18.5^\circ$ , w/brackets

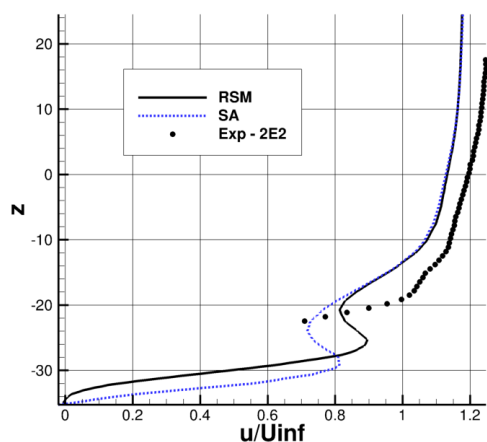
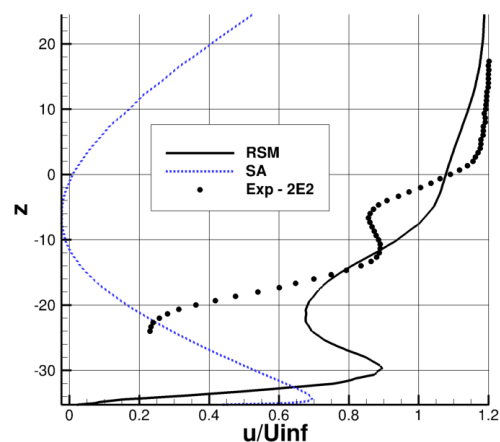
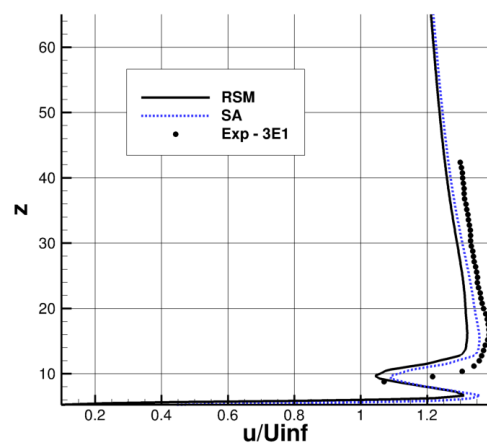
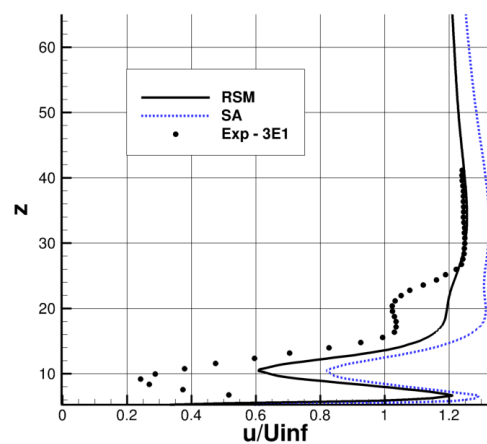
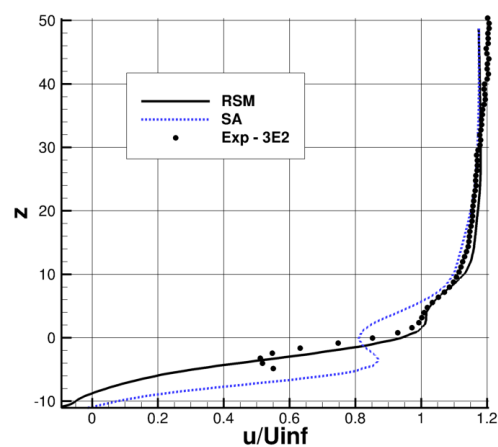
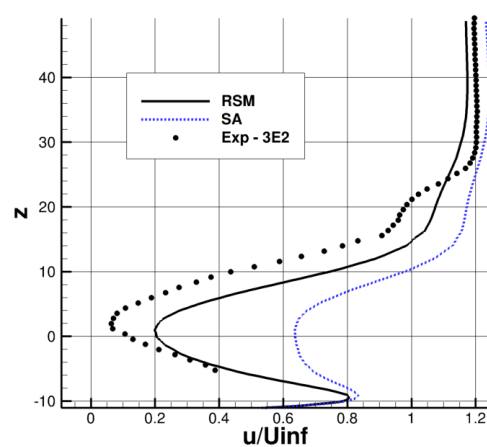


(e) Location 2E1 at  $\alpha = 7^\circ$ , w/brackets



(f) Location 2E1 at  $\alpha = 18.5^\circ$ , w/brackets

**Figure 13. Velocity profiles (part 2) at  $Re = 1.35 \times 10^6$**

(a) Location 2E2 at  $\alpha = 7^\circ$ , w/brackets(b) Location 2E2 at  $\alpha = 18.5^\circ$ , w/brackets(c) Location 3E1 at  $\alpha = 7^\circ$ , w/brackets(d) Location 3E1 at  $\alpha = 18.5^\circ$ , w/brackets(e) Location 3E2 at  $\alpha = 7^\circ$ , w/brackets(f) Location 3E2 at  $\alpha = 18.5^\circ$ , w/brackets**Figure 14. Velocity profiles (part 3) at  $Re = 1.35 \times 10^6$**

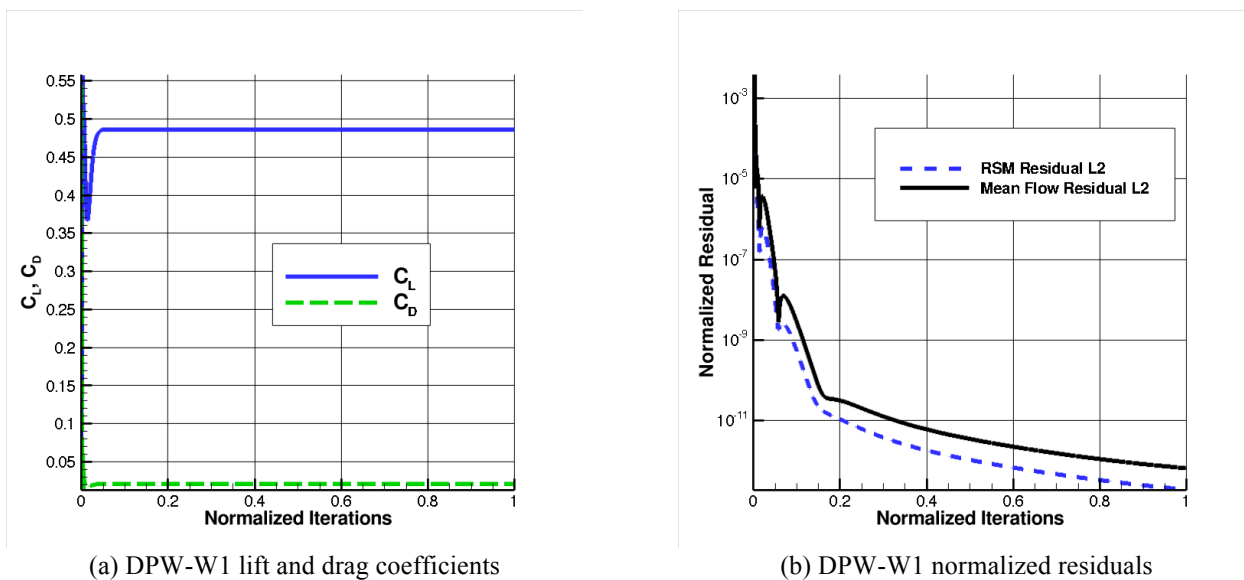


Figure 15. Representative convergence information for DPW-W1

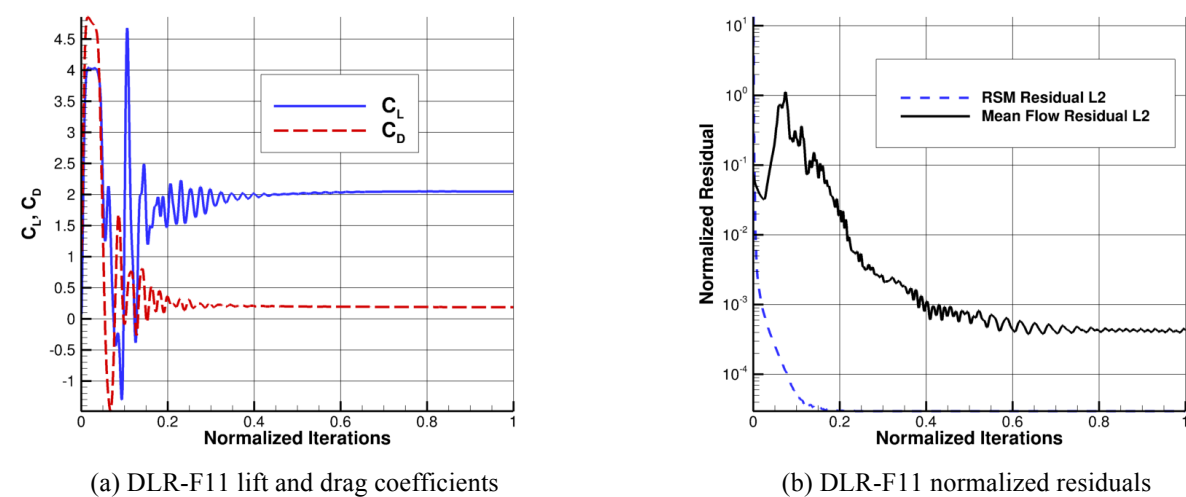


Figure 16. Representative convergence information for DLR-F11 (high Re, no brackets),  $\alpha = 7^\circ$